JGR Oceans

RESEARCH ARTICLE
10.1029/2018JC014737

Toward Realistic Nonstationarity of Semidiurnal Baroclinic Tides in a Hydrodynamic Model

Arin D. Nelson[1], Brian K. Arbic[1], Edward D. Zaron[2], Anna C. Savage[3,4], James G. Richman[5], Maarten C. Buijsman[6], and Jay F. Shriver[7]

[1]Department of Earth and Environmental Sciences, University of Michigan, Ann Arbor, MI, USA, [2]Department of Civil and Environmental Engineering, Portland State University, Portland, OR, USA, [3]Applied Physics Program, University of Michigan, Ann Arbor, MI, USA, [4]Scripps Institution of Oceanography, University of California, San Diego, La Jolla, CA, USA, [5]Center for Oceanic-Atmospheric Prediction Studies, Florida State University, Tallahassee, FL, USA, [6]Division of Marine Sciences, University of Southern Mississippi, Hattiesburg, MS, USA, [7]Oceanography Division, Naval Research Laboratory, Stennis Space Center, Hancock County, MS, USA

Key Points:
- Hydrodynamic models incorporating mesoscale dynamics and tides are beginning to resolve stationary and nonstationary baroclinic tides
- The ratio of nonstationary to total semidiurnal variance computed from altimetry and HyCOM simulations agrees at low and middle latitudes
- Comparisons of analysis methodologies show that total and nonstationary semidiurnal variances are underestimated in altimetry on average

Correspondence to:
A. D. Nelson,
dr.adnelson@gmail.com

Citation:
Nelson, A. D., Arbic, B. K., Zaron, E. D., Savage, A. C., Richman, J. G., Buijsman, M. C., & Shriver, J. F. (2019). Toward realistic nonstationarity of semidiurnal baroclinic tides in a hydrodynamic model. *Journal of Geophysical Research: Oceans*, *124*, 6632–6642. https://doi.org/10.1029/2018JC014737

Received 2 NOV 2018
Accepted 1 AUG 2019
Accepted article online 30 AUG 2019
Published online 10 SEP 2019
Corrected 17 DEC 2019

This article was corrected on 17 DEC 2019. See the end of the full text for details.

Abstract Semidiurnal baroclinic tide sea surface height (SSH) variance and semidiurnal nonstationary variance fraction (SNVF) are compared between a hydrodynamic model and altimetry for the low- to middle-latitude global ocean. Tidal frequencies are aliased by ~10-day altimeter sampling, which makes it impossible to unambiguously identify nonstationary tidal signals from the observations. In order to better understand altimeter sampling artifacts, the model was analyzed using its native hourly outputs and by subsampling it in the same manner as altimeters. Different estimates of the semidiurnal nonstationary and total SSH variance are obtained with the model depending on whether they are identified in the frequency domain or wavenumber domain and depending on the temporal sampling of the model output. Five sources of ambiguity in the interpretation of the altimetry are identified and briefly discussed. When the model and altimetry are analyzed in the same manner, they display qualitatively similar spatial patterns of semidiurnal baroclinic tides. The SNVF typically correlates above 80% at all latitudes between the different analysis methods and above 60% between the model and altimetry. The choice of analysis methodology was found to have a profound effect on estimates of the semidiurnal baroclinic SSH variance with the wavenumber domain methodology underestimating the semidiurnal nonstationary and total SSH variances by 68% and 66%, respectively. These results produce a SNVF estimate from altimetry that is biased low by a factor of 0.92. This bias is primarily a consequence of the ambiguity in the separation of tidal and mesoscale signals in the wavenumber domain.

1. Introduction

The identification and removal of the internal tide sea surface height (SSH) signal are a first-order problem in satellite altimetry. Compared to the relatively large scale barotropic tides, baroclinic tides (also called internal tides) have a small SSH amplitude (order of centimeters), are spatially short (order of 100 km), and are significantly affected by ocean stratification and mesoscale currents, making them intrinsically difficult both to discern in altimetry observations and to predict with hydrodynamic models. However, the removal of baroclinic tides from altimetry is critical for distinguishing nontidal phenomena, and ocean models are increasingly becoming an essential tool in this endeavor. The removal of internal tides will be especially important for the Surface Water and Ocean Topography (SWOT) wide-swath altimeter mission planned to launch in 2021 (Fu et al., 2012), which will perform measurements at smaller length scales than any previous altimeter mission.

Currently, baroclinic tides are included in several models such as the Hybrid Coordinate Ocean Model (HyCOM; Arbic et al., 2010; Arbic et al., 2012; Arbic et al., 2018), the MIT General Circulation Model (MITgcm; e.g., Rocha, Gille, et al., 2016; Rocha, Chereskin, et al., 2016), the German STORMTIDE model (e.g., Müller et al., 2012), the Nucleus for European Modeling of the Ocean community model (Madec, 2008), and the Geophysical Fluid Dynamics Laboratory (GFDL) Generalized Ocean Layered Dynamics model (GOLD; e.g., Waterhouse et al., 2014). Some regional baroclinic tide models exist as well (e.g., Kelly et al., 2016). In fact, it is only recently that computing power has progressed enough to feasibly allow global ocean models to run at the high spatial and temporal resolutions necessary to resolve baroclinic tides.

Baroclinic tides are created when barotropic tidal currents pass over sloping topography, generating internal waves that are phase-locked with the tidal forcing (Kelly et al., 2010). These phase-locked internal waves are referred to as stationary tides since they can be written in terms of a known amplitude and phase and are hence predictable. Internal tides may lose their phase relationship with the barotropic forcing as they interact with topography (e.g., Duda et al., 2012; Klymak et al., 2016), as they propagate through time variable ocean stratification (e.g., Buijsman et al., 2017) or by interacting with subtidal flows including eddies and currents (e.g., Dunphy & Lamb, 2014; Dunphy et al., 2017; Kelly & Lermusiaux, 2016). These are called nonstationary tides, and they are less predictable by nature. Hydrodynamic models that are able to simulate internal tides along with mesoscale and submesoscale dynamics should also simulate nonstationary internal tides, meaning it may be possible for them to aid in predicting nonstationary tides for future altimetry missions. Motivated by this, the percent variance of the semidiurnal (twice daily) internal tides that is nonstationary in a hydrodynamic model will be computed in this paper and compared with the same quantity computed from altimetry.

Although their temporal resolution is relatively coarse, altimeter observations have been used to study global baroclinic tides (Ray & Mitchum, 1996, 1997; Ray & Zaron, 2016; Zhao et al., 2016). With a temporal resolution on the order of 10 days, altimeters alias the tides and other high-frequency motions onto lower frequencies. To circumvent the issue of aliasing, tidal analyses using altimetry are often performed in the wave number domain. The differences caused by the choice of analysis in either the frequency or wave number domain have not yet been quantified in the context of ocean tides. In this work, we use both methodologies to analyze model output with a sufficiently high temporal resolution to investigate this quandary.

Several studies exist where altimeter observations are used to gauge the fidelity of global simulations containing baroclinic tides (Ansong et al., 2015; Arbic et al., 2012; Müller et al., 2012; Shriver et al., 2012), of which all but Müller et al. (2012) focused on HyCOM. These studies found that the spatial averages of stationary tidal amplitudes in HyCOM agreed well with observations in "hot spot" regions of large internal tide generation but did not agree as well in regions of strong mesoscale activity and/or small tidal amplitudes (Shriver et al., 2012). This study goes one step further by comparing the nonstationary tidal amplitudes and semidiurnal nonstationary variance fraction (SNVF) on basin and global scales.

No matter if the analysis is done in the frequency or wave number domain, SNVF is determined by computing the spectra before and after the stationary tides have been subtracted from the time series, integrating over the semidiurnal internal tide frequency or wave number band then computing the ratio of the nonstationary to total semidiurnal variance. This procedure for computing SNVF is relatively easy to perform in the frequency domain since the tides and other physical features (e.g., mesoscale eddies) have clearly separate time scales. However, in the wavenumber domain, internal tides and mesoscale eddies have similar length scales, and there is ambiguity on how to separate these signals. This leads to a number of subjective choices that will be identified and discussed. The model is sufficiently resolved to use both methodologies, allowing for the identification of limitations and biases in the wave number domain methodology. Implications of these limitations and biases for past and future altimetry missions will be briefly explored.

2. Data and Methods

The objective of this paper is to assess the nonstationary tides within a state-of-the-art ocean model by comparing them with data available from satellite altimetry. By definition, the nonstationary tide refers to a signal that originates from the tide generating force but is not phase-locked to this forcing. This definition corresponds most logically with an analysis method that first identifies the stationary tide by harmonic analysis—identifying the signal component that is phase-locked to the tidal forcing—and then identifies the residual signal within a given frequency bandwidth around the known tidal frequencies. Thus, the identification of the nonstationary tide is most naturally accomplished in the frequency domain. While it is feasible to analyze the tides in the hourly output of a numerical model using this methodology (Buijsman et al., 2017; Savage et al., 2017), which shall be referred to as the "f-space" (frequency-space) methodology, it is not feasible to apply this to altimeter data. Various approaches have been employed to identify nonstationary tides from altimetry, but ambiguity is introduced by the limitations inherent in the sampling of altimeters which alias the tidal frequencies (Zhou et al., 2015, 2017; Zaron, 2015). The method used in this paper shall be referred to as the "k-space" (wavenumber-space) methodology, since it infers the nonstationary tide from the wave number spectrum, rather than the frequency spectrum.

In this section the k-space methodology that was originally used with altimetry is described in detail. The key to the comparison of model and data in this study is to use the k-space methodology on the model output, after subsampling to match the altimetry. Additionally, though, the native-resolution model output permits the separate comparison of the k-space and f-space methodologies, solely from model output, in order to identify likely errors and biases in the k-space approach—a comparison which is not possible from analysis of altimeter data alone.

2.1. Altimetry

The altimeter data and analysis methodologies used in this study come from Zaron (2017). The data consist of the combined 23 years of TOPEX/Poseidon, Jason-1, and Jason-2 (T/P-J) altimeter measurements with all standard corrections applied, including environmental path delays, the inverse barometer effect, sea-state bias, mean sea level, solid Earth tides, and barotropic tides. From these data, 2,000-km-long track segments centered at each ascending and descending track cross-over point were collected. For data near land, tracks shorter than 1,200 km or with gaps greater than 30 km were rejected.

The orbit repeat time of the T/P-J altimeters is 856,712 s (9.91565 days) on average (Benada, 1997). Because of this, traditional f-space analyses cannot easily distinguish tidal motions in altimeter data since all sources of variability with frequencies shorter than half the altimeter sampling frequency will be aliased onto lower frequencies. This orbit repeat time was chosen so that tidal aliases would not overlap with significant periods of climate variability such as the seasonal cycle, annual cycle, or longer periods. Even so, tens or sometimes even hundreds of altimeter passes are needed to reliably separate tidal variability from other motions (see, e.g., the tidal aliasing periods associated with the T/P-J missions in Table 3 of Ray, 1998). Therefore, the along-track analysis of internal tides from altimetry is typically performed in k-space. The k-space analysis method of Zaron (2017), which is based upon methods in Ray and Zaron (2011), will be summarized here.

First, an estimate of nontidal variability was subtracted from the SSH anomaly relative to the record length mean SSH to reduce the amount of nontidal mesoscale variability. This "mesoscale correction" was performed by subtracting the SSH fields from the Archiving, Validation, and Interpretation of Satellite Oceanographic Data center's Data Unification and Altimeter Combination System version DT-2014 (Pujol et al., 2016). This mesoscale correction was also used in Ray and Zaron (2016) and Zaron (2017), although it has been noted that there is some leakage of internal tide variability in this Archiving, Validation, and Interpretation of Satellite Oceanographic data (Zaron and Ray (2018); also see the Appendix of Ray & Zaron, 2016). Even with this contamination, this mesoscale correction was found to be essential for identifying internal tidal signals in the temporally aliased altimeter data.

From this "corrected" data, the stationary tide was identified and removed from each time series using harmonic analysis. k-space power spectral densities were then computed along each track for each altimeter cycle from both the total and stationary tide-subtracted (or nonstationary) SSH data with Hann windows applied. These spectra were then averaged over all cycles. It should also be noted that, contrary to some previous works (e.g., Ray & Zaron, 2016), no high-pass spatial filter was applied to the along-track data at any point during this analysis. The high-pass filter used in these works was originally used to remove mesoscale eddies and other larger-scale features, but it was found to remove some tidal variability as well, hence our choice to neglect this operation.

In Zaron (2017), the SSH k-space spectra were shown to consist mainly of a broadband continuum besides a bump around the baroclinic wave numbers and a white noise-like spectrum at short wavelengths ($\leq$30 km). The noise level was defined by averaging the k-space spectra beyond this limit, and the broadband continuum was modeled as a low-order polynomial.

The variance associated with the Mode 1 semidiurnal internal tides is estimated by integrating the variance under the spectral bump. The relatively short length of the along-track segments does not permit resolution of the wave number peaks associated with individual tidal frequencies in the semidiurnal band (e.g., M2, S2, and N2); therefore, the integrated variance is a sum of all these components. Since the M2 tide is generally the largest amplitude, the wavelength of the Mode 1 M2 tide, denoted k_{M2}, is used to locate the peak, and variance is computed by integrating between wavenumbers k_1 and k_2, $k_1 \leq k_{M2} \leq k_2$, defined by the local minima in the corrected spectrum closest to k_{M2}. The white noise and broadband variances between these wave numbers were also computed and subtracted, resulting in "residual" total and nonstationary variances.

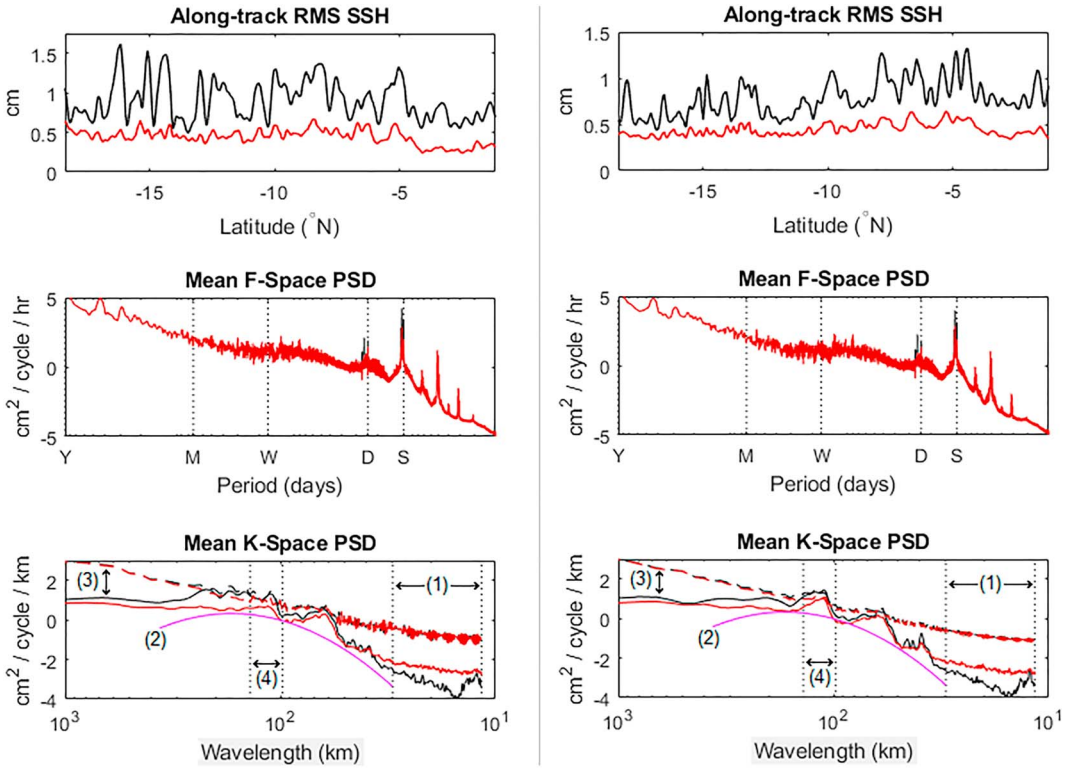

Figure 1. Along-track analysis of the altimeter-sampled Hybrid Coordinate Ocean Model output from the Southeast Atlantic centered on 10°S, 3°W for the (left column) ascending track and (right column) descending track. (top row) Total (black) and nonstationary (red) semidiurnal RMS SSH values at each point along each track. (middle row) Mean *f*-space power spectral density (PSD) from each model output hourly time series along each track. Vertical dotted lines are plotted at yearly (Y), monthly (M), weekly (W), diurnal (D), and semidiurnal (S) frequencies. (bottom row) Mean *k*-space power spectral density from each altimeter-sampled track, including spectra for the total SSH (black), the nonstationary SSH (red), and the broadband model (magenta). The dashed lines are the spectra when the mesoscale/nontidal variability is not removed. The four numbers/regions label the first four of the five subjective choices of the *k*-space analysis method listed in the text. The uncertainty of the stationary tidal fit causes the increase in variance in the low wave numbers of the nonstationary SSH spectrum relative to the total SSH spectrum. RMS = root-mean-square; SSH = sea surface height.

The SNVF was then computed by dividing the residual nonstationary variance by the residual total variance. See Figure 1 for an application of this methodology at a single altimeter cross-over.

The distinction between stationary and nonstationary variance is reasonably straightforward when time-resolved SSH is analyzed in the frequency domain (e.g., Colosi & Munk, 2006); however, the above-described methodology involves potentially problematic, and subjective, choices to deal with the altimeter temporal aliasing and relatively small signal-to-noise level. These choices include the definition of (1) the white noise and (2) broadband spectra, (3) the mesoscale correction method, (4) the choice of integration limits, and (5) how the variance estimates from the ascending and descending tracks were reconciled into a single value. In order to reproduce the analysis of Zaron (2017), we had to replicate their choices as closely as possible; these choices will be discussed in the results. The five subjective choices used by Zaron (2017) were used when performing the *k*-space analyses of the model data, with one small difference; the mesoscale correction for the model was performed by subtracting the weekly running mean from every time series, replicating a "perfect" implementation of the mesoscale correction methodology applied by Zaron (2017).

2.2. Model Output

This work uses 5 years of hourly steric SSH output from a HyCOM simulation managed by the Naval Research Laboratory run on a tripolar spatial grid with a nominal spacing of (1/12.5)° near the equator. In addition to the standard atmospheric forcing fields, this simulation included forcing at the four strongest diurnal tides (K_1, O_1, P_1, and Q_1) and the four strongest semidiurnal tides (K_2, M_2, N_2, and S_2). Steric SSH

instead of total SSH was used since it does not contain barotropic motions. See the Appendix of Savage et al. (2017) for a discussion of the procedure used to compute steric SSH in HyCOM.

The output from this simulation was used in Shriver et al. (2012) and numerous studies thereafter (Richman et al., 2012; Timko et al., 2012, 2013). There are newer HyCOM tide simulations having higher spatial resolution (e.g., (1/25)° as in Savage et al., 2017) and more accurate barotropic tides (e.g., Ngodok et al., 2016), but the older simulation was used because of its longer output duration (5 years as opposed to 1 year in other simulations, including Savage et al., 2017). The longer output was essential when analyzing the altimeter-sampled model output because altimeter sampling provides only about 72 tracks per cross-over point per year, and longer time series of SSH have been shown to produce better estimates of nonstationarity (Ansong et al., 2017).

Because the output of the HyCOM simulation was saved hourly, it is feasible to compute the tidal statistics using the f-space methodology, defined as integrating the frequency power spectral densities of the total and nonstationary SSH time series between 1.85 and 2.05 cycles per day (Savage et al., 2017) at the model grid point closest to the respective altimeter cross-over point. However, it is important to process and analyze the model output in the same fashion as the observations in order to obtain the most reasonable comparison between the two. In this case, the hourly model output was sampled using the spatial pattern of sampling along the T/P-J tracks (Benada, 1997). Additionally, having both hourly and altimeter cycle time series allows us to compute the tidal statistics using three possible methodologies:

1. k-space of the altimeter tracks sampled once per altimeter cycle,
2. k-space of the hourly altimeter tracks, and
3. f-space of the hourly time series averaged over all altimeter points.

The first analysis is the best analog to that used in the observations, so the results of this analysis are the best choice for comparing the model output to the observations. The second analysis will be used to investigate how the temporal sampling of the altimeters affects the k-space results. The last analysis will be used to investigate possible biases in using the k-space methodology in place of the f-space methodology when both methodologies are feasible.

3. Results

3.1. Analyses at a Single Location

To validate our analysis procedures, we applied them to altimeter-sampled HyCOM tracks corresponding to the six regional analyses defined in section 4 of Zaron (2017). These locations have varying strengths of mesoscale variability, stationary tides, and nonstationary tides. For brevity, the results of only one test location will be shown here: the cross-over point located at 10°S, 3°W in the Southeast Atlantic. This location was chosen for this discussion since it contains moderate strengths of both tidal and nontidal variability. The results of these analyses are displayed in Figure 1. The five subjective choices in the k-space methodology listed at the end of section 2.1 will now be discussed:

1. Noise removal. Zaron (2017) and others have noted the presence of a pervasive white noise spectrum that can be characterized using the high-wavenumber portion of the spectrum. For this work, the white noise region was defined akin to Zaron (2017) at wavelengths lower than 30 km. Since this white noise spectrum is subtracted from the full spectrum, the subjective choice of how to define the white noise spectrum could affect the later variance estimates. The noise is generally much smaller than the variances of interest in the altimeter data and is almost nonexistent in the model, so the results are the least sensitive to this choice among the five.
2. Broadband removal. The broadband spectrum differs greatly with location (see, e.g., Figure 2 of; Zaron, 2017). Additionally, the mesoscale correction can significantly affect the shape of the broadband spectrum. This makes it tricky to choose a satisfactory global definition for the broadband spectrum. In this work, an order-two polynomial was chosen to account for any curvature in the broadband while limiting any overfitting that could occur when using higher-order polynomials.
3. Mesoscale/nontidal variability removal. The choice of mesoscale model to remove nontidal variability from altimeter-sampled results is another complexity. As has been shown, even utilizing an imperfect mesoscale model is important in clearly identifying the stationary internal tides (e.g., Ray and Zaron (2016)). For the altimeter-sampled model output, a weekly running average was subtracted from all time

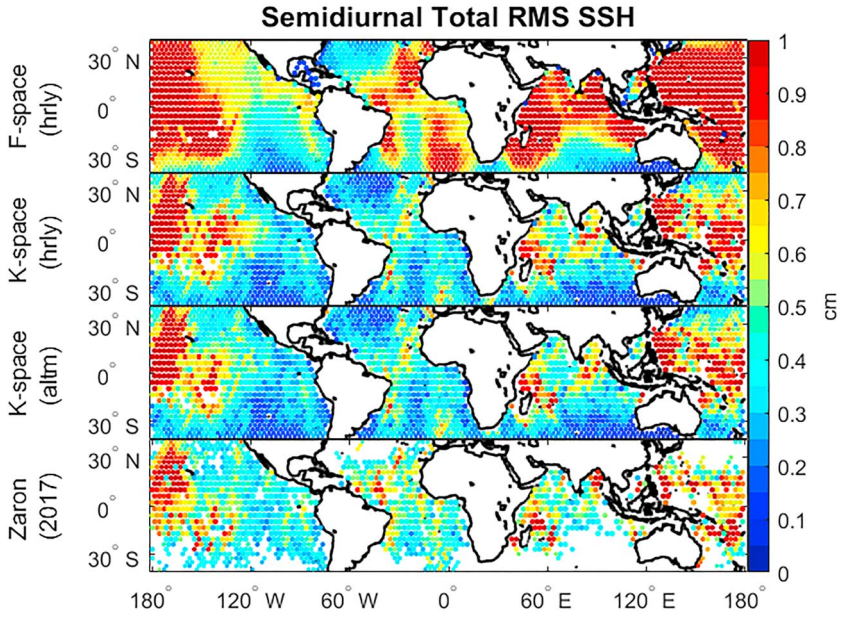

Figure 2. Global maps of semidiurnal total SSH variability (RMS anomaly). The top three maps are computed from the Hybrid Coordinate Ocean Model 1/12.5° 5-year run using (first) f-space methodology applied to the hourly output, (second) k-space methodology applied to the hourly output, and (third) k-space methodology applied to the altimeter-sampled output. These are plotted alongside (fourth) the results from altimetry in Zaron (2017). In all subplots, results are only plotted where the total semidiurnal variance σ_T^2 is greater than twice the error variance σ_E^2. RMS = root-mean-square; SSH = sea surface height.

series to mimic a perfect mesoscale model following the characteristics of the mesoscale model used in Zaron (2017).

4. Choice of integration limits. At many locations, the local stationary tide is a sum of propagating stationary tidal waves from multiple sources. If the tides propagate at a high angle relative to the altimeter track (see, e.g., Figure 6 in Ray and Zaron (2016)), there may be multiple peaks in the wave number spectrum that may or may not reside within the integration limits of the Mode 1 wavenumber k_{M2}. For example, the bottom subplot in Figure 1 shows multiple peaks beyond 100 km in the total SSH spectrum but not the nonstationary SSH. This indicates that there are sources of nonstationary tides propagating at large angles relative to the altimeter track, which manifests as variance at wavelengths beyond the k_{M2} band as defined in this work. Following previous works, the integration limits were chosen to be the local minima surrounding only the peak in the wave number spectrum closest to k_{M2}, meaning that the semidiurnal variances at some locations may be grossly underestimated.
5. Reconciling results from the two tracks. In this work, the variance estimates from the ascending track and descending track are averaged to give a single value for the variance at each cross-over point. As mentioned in the discussion of the choice of integration limits, the k-space spectrum from the descending track contains a majority of its stationary semidiurnal variance between the local minima surrounding the peak nearest the k_{M2} peak, while ascending track k-space spectrum contains a significant amount of variance outside the k_{M2} integration limit at longer wavelengths. Since the variance estimates from the two tracks are averaged, the missing variance in the ascending track's variance estimate constitutes an as-of-yet unresolved error in the concluding variance estimate at this cross-over location.

3.2. Semidiurnal Variances and Variance Ratios

Figures 2 to 4 display global maps of the total and nonstationary semidiurnal band SSH variabilities and SNVF for the three different methodologies listed in section 2.2 along with the results from altimetry in Zaron (2017). At a cursory glance, all analyses show similar qualitative features. In the maps of nonstationary semidiurnal SSH variability (Figure 3), there is a large band of nonstationarity in the equatorial Pacific Ocean, due to the equatorial crossings of the stationary tides generated near Hawaii, near the Philippines, and in the tropical South and southwest Pacific. This is consistent with the analysis of the HyCOM simulation studied by Buijsman et al. (2017). There is additionally a large amount of nonstationarity in

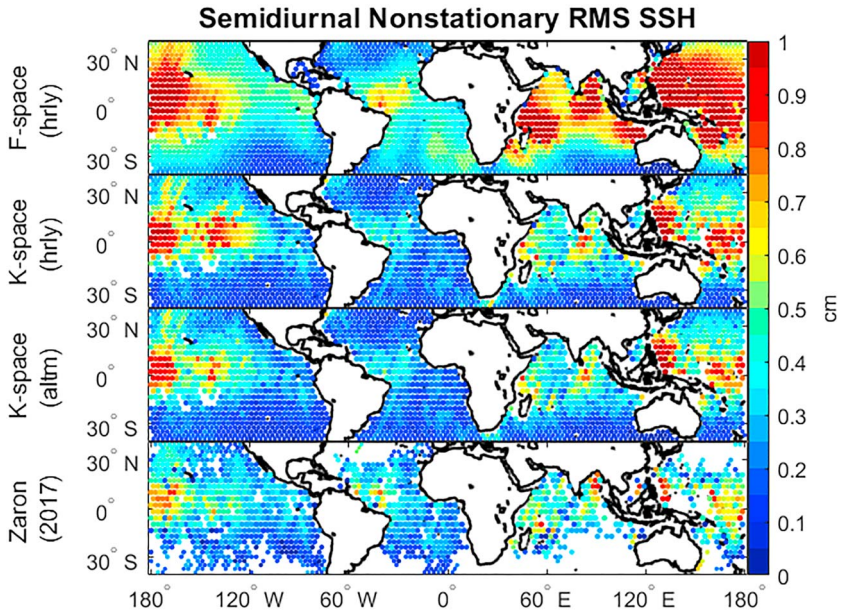

Figure 3. As in Figure 2 but for semidiurnal nonstationary SSH variability.

the Indian Ocean where the stationary tides generated near Madagascar cross the Mascarene Plateau, the Chagos-Laccadive Ridge, and the Ninety East Ridge as they propagate further eastward. There is also strong nonstationarity in regions of high mesoscale variability (e.g., boundary currents), where the mesoscale dynamical features (e.g., eddies) refract and scatter the internal tide. Additionally, as also found in Zaron (2017), low semidiurnal tidal variances and high observational uncertainties poleward of 40° caused the analysis to be restricted to equatorward of 40°. In all figures, data are only plotted where the total semidiurnal variance σ_T^2 is greater than twice the error variance σ_E^2. In the model, this error is almost zero.

The major discrepancy in these results is that the *k*-space method tends to underestimate both nonstationary and total semidiurnal variances. Conversely, the *k*-space method differs marginally when applied to 10-day sampled model output versus the original hourly output of the model, which is unsurprising as the altimeter repeat time was chosen specifically to minimize the temporal aliasing on the tides, and a 3-year span was found to be satisfactory for capturing semidiurnal stationary tides (Ray & Zaron, 2011). The discrepancy in the *f*-space and *k*-space results stems from a combination of the five subjective parameters in the *k*-space method listed previously, the effects of which vary strongly with location. The global area-weighted average ratio of the nonstationary semidiurnal variance from the *k*-space methodology (0.12 cm^2) versus that from the *f*-space methodology (0.37 cm^2) is 0.32. For the total semidiurnal variance, the ratio of the *k*-space estimate (0.26 cm^2) to the *f*-space estimate (0.77 cm^2) is 0.34. This highlights the importance of processing and analyzing observational data and model outputs as similarly as possible for the comparisons between the two to be meaningful. If the *f*-space methodology applied to the hourly data (e.g., this work, or the results of Savage et al., 2017), were compared directly to altimetry, the model would appear to be grossly overestimating semidiurnal baroclinic variances, especially in the Indian Ocean and central and western Pacific Ocean. However, the *k*-space method applied to the altimeter-sampled model output agrees much better with the altimetry, showing more similar spatial patterns and variance magnitudes, with the model only slightly overestimating the semidiurnal baroclinic variances.

Perhaps most surprising is the similarities in the SNVF across analysis methods. Qualitatively, all three methodologies applied to the model output show very similar spatial patterns and SNVF values, all of which also appear to agree well with the results from altimetry. This robustness in the comparison of the variance ratios versus the individual variances was quantitatively assessed by computing the correlations between the various variances and SNVF across the different methods in 10° latitude bins. These correlations are displayed in Figure 4. All correlations are statistically significant to at least 95% confidence. Across all three comparisons, the SNVF has the highest correlation between analysis methods averaged across all

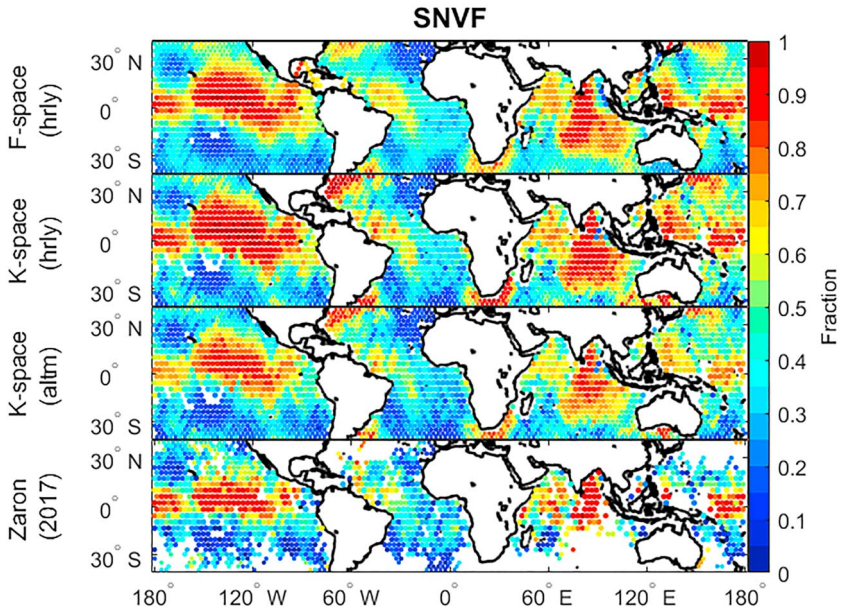

Figure 4. As in Figure 2 but for SNVF. SNVF = semidiurnal nonstationary variance fraction.

latitudes. For all analysis methods and correlations from the model output, there is no discernible pattern versus latitude.

Between the model output and altimetry, the semidiurnal total SSH variance is consistently correlated versus latitude at 0.5–0.6 in the equatorial ocean and at 0.7–0.8 in the northern midlatitude ocean. Semidiurnal nonstationary SSH variance correlates most well along the equator and lessens as latitude increases poleward. This is due to how the nonstationary tides are generated in these two regimes. Stationary tides propagating across the equator are mainly scattered by the change in ocean stratification and equatorial currents (Buijsman et al., 2017), which are relatively broad scale and thus well simulated in the model. At higher latitudes, nonstationary tides are primarily generated by dynamical features such as eddies and western boundary currents. The HyCOM simulation did not include data assimilation, so the locations of these features, and thus the spatial distribution of the nonstationarity, may be mismatched relative to what was seen in altimetry. Surprisingly, even with these discrepancies in the stationary and nonstationary variances, the SNVF ratio stays relatively consistent across latitudes, although the correlations are slightly higher near the equator.

4. Discussion

As global ocean models such as HyCOM have attained progressively more realism through improved resolution and representation of atmospheric and tidal forcing, the related tasks of calibration and validation have proceeded stepwise, through model-data intercomparison of separate physical phenomena such as mesoscale kinetic energy (Thoppil et al., 2011), mesoscale available potential energy (Luecke et al., 2017), and tidal SSH variability (Ansong et al., 2015; Shriver et al., 2012). In this paper, we seek to validate a model's nonstationary tide, which arises as a joint phenomenon of the tides and mesoscale dynamics simultaneously. The motivation for this study is both to understand whether the model's representation of the interaction between these phenomena is adequate and to establish a benchmark of skill for comparison of future efforts which will likely seek to forecast the nonstationary tide in the context of the SWOT swath altimeter mission (Fu et al., 2012).

A key finding of the present study is the degree to which the wavenumber-space (*k*-space) methodology underestimates the nonstationary tidal SSH variance. Assuming that the model is accurate enough to be used as a guide, a comparison of the *f*-space and *k*-space methodologies finds that the latter is biased low and

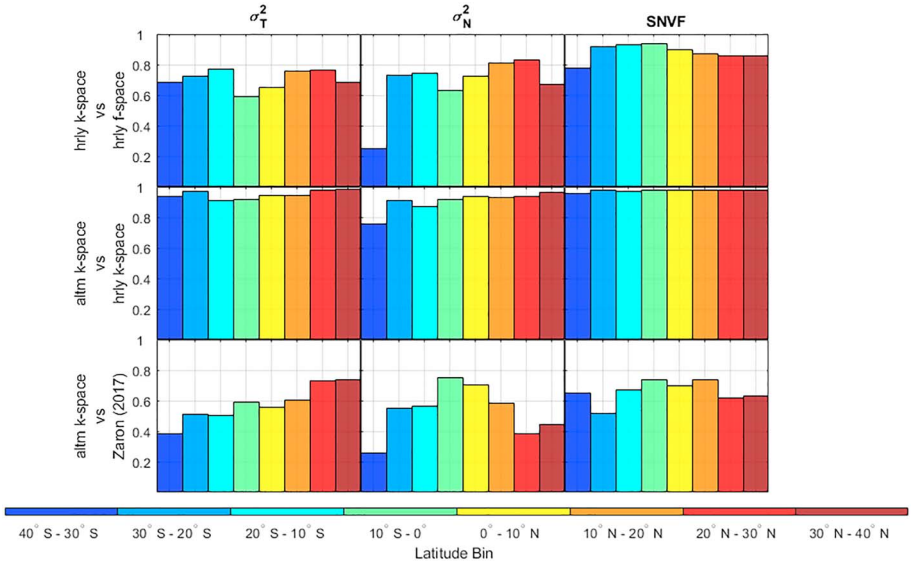

Figure 5. Correlations between the estimates of the semidiurnal variances of the total σ_T^2 and nonstationary σ_N^2 sea surface height and their ratio, the semidiurnal nonstationary variance fraction, between the three methodologies over 10° latitude bins.

misses a large fraction of the nonstationary variance (cf., top two panels of Figure 3). The *k*-space methodology was developed to overcome the effects of altimeter aliasing, but its implementation relies on several procedures, the validity of which cannot be tested from altimeter data alone. These procedures include (in order from least to most significant) the estimation and removal of a white noise instrumental error spectrum, correction for the mesoscale/nontidal SSH variability, estimation and removal of a broadband mesoscale/nontidal spectrum, choice of integration limits defining the nonstationary spectrum bandwidth, and accounting for nonisotropy by averaging spectra from ascending and descending tracks. Zaron (2017) highlighted the role played by the assumed broadband mesoscale/nontidal spectrum and noted that if this broadband spectrum consisted of a steeply sloped spectrum, for example, k^{-3}, buried "underneath" the tide-dominated spectrum, then the nonstationary variance could be much larger than the values inferred there. Indeed, the present study indicates that this is the case. The ratio of the area-weighted global average of the semidiurnal nonstationary variance obtained with the *k*-space analysis (0.12 cm^2) with the *f*-space analysis (0.37 cm^2) is found to be 0.32. For the semidiurnal total variance, the ratio of the variance from the *k*-space analysis (0.26 cm^2) to the *f*-space analysis (0.77 cm^2) is 0.34. However, the ratio of the area-weighted global average SNVF from the *k*-space analysis (0.45) to that from the *f*-space analysis (0.49) is 0.92.

Because the *k*-space analysis produces biased estimates of both the nonstationary and the total tidal variance, their ratio, the SNVF, is relatively well correlated between the model and the altimetry (cf., Figure 4). This positive correlation, and the map of Figure 5, suggests that HyCOM is accurately representing the interactions of the baroclinic tides and mesoscales; however, as the preceding paragraph makes clear, the altimeter data provide relatively weak constraints for describing the nonstationary tide—at least using the data and methods presently in the literature. The challenge with validating a global model such as HyCOM is the trade-off between temporal and spatial resolution inherent in most data sources. Analysis of stationary and nonstationary tides using data from surface drifters is currently being investigated to overcome some of the limitations of altimetry data (Elipot et al., 2016).

5. Summary

In order to compare and validate ocean model results with observed data, it is necessary to implement ocean model analysis procedures that match the procedures used in the observations. This matched approach has been taken on in order to compare the nonstationary tides simulated with a combined tides-and-mesoscale-resolving HyCOM simulation with the nonstationary tides inferred using satellite altimetry. The comparison finds that the steric height variance associated with baroclinic tides is considerably larger in the model than in the data; however, the ratio of nonstationary to total tidal variance, denoted SNVF, is spatially correlated between the model and data.

These results were rationalized by examining carefully the statistics of the nonstationary tide in different subsamples of the model output, as they were progressively degraded from the native resolution of the model to the coarser resolution of the altimetry. The notion of nonstationary tidal variance, which is unambiguously defined in the frequency domain, is not clearly defined in the wavenumber domain and complicates the analysis of altimetry data. Assuming that the HyCOM results are accurate enough to be used as a guide, the globally averaged altimeter-based estimates of the nonstationary and total semidiurnal variances are only 0.32 and 0.34 of their true values, respectively. In other words, the altimeter underestimates the magnitude of the nonstationary and total semidiurnal variances by 68% and 66%, respectively, on average. Additionally, the SNVF is biased low by a factor of 0.92.

The spatial correlation of nonstationary tidal variance in the model with that inferred from altimetry suggests that the model is capturing a significant part of the interaction between baroclinic tides and the mesoscale circulation. A more comprehensive evaluation of the nonstationary tides in HyCOM is challenged by the lack of global data sets with the temporal resolution and duration necessary to resolve tidal variability. Future validation efforts might consider comparison of the rates of water mass transformation and mixing driven by the dissipation of the internal tide. Although this is a higher-order quantity further removed from the tidal forcing and air-sea exchange, the integrative nature of water mass properties might make them straightforward to compare between model output and in situ data.

Acronyms

HyCOM	Hybrid Coordinate Ocean Model
MITgcm	Massachusetts Institute of Technology general circulation model
GFDL	Geophysical Fluid Dynamics Laboratory
GOLD	Generalized Ocean Layered Dynamics
SWOT	Surface Water and Ocean Topography
SSH	Sea surface height
SNVF	Semidiurnal nonstationary variance fraction

Acknowledgments
The HyCOM outputs used in this study were obtained under the FY09-11 Department of Defense HPC Challenge Project Eddy Resolving Global Ocean Prediction including Tides and were provied by J. F. S. (Shriver et al., 2012). The satellite altimeter data used in this study were extracted from the RADAR Altimetry Database System (RADS; http://rads.tudelft.nl/rads/rads.shtml) and processed by E. D. Z. (Zaron, 2017). A. D. N., B. K. A., J. F. S., M. C. B., J. G. R., and A. C. S. are grateful for support from the NASA Grants NNX17AH55G and NNX16AH79G as well as the Office of Naval Research Grant N00014-15-1-2288. E. D. Z. acknowledged funding provided by the NASA Award NNX16AH88G. A. C. S. acknowledges funding provided by the NASA Earth and Space Science Fellowship Grant NNX16AO23H. B. K. A. and A. C. S. acknowledge funding by the University of Michigan Associate Professor Support Fund, supported by the Margaret and Herman Sokol Faculty Awards. This NRL contribution NRL/JA/7320-19-4560 has been approved for public release. The authors would also like to thank the two anonymous reviewers for their help in strengthening this paper.

References

Ansong, J. K., Arbic, B. K., Alford, M. H., Buijsman, M. C., Shriver, J. F., Zhao, Z., et al. (2017). Semidiurnal internal tide energy fluxes and their variability in a global ocean model and moored observations. *Journal of Geophysical Research: Oceans*, *122*, 1882–1900. https://doi.org/10.1002/2016JC012184

Ansong, J. K., Arbic, B. K., Buijsman, M. C., Richman, J. G., Shriver, J. F., & Wallcraft, A. J. (2015). Indirect evidence for substantial damping of low-mode internal tides in the open ocean. *Journal of Geophysical Research: Oceans*, *120*, 6057–6071. https://doi.org/10.1002/2015JC010998

Arbic, B., Alford, M. H., Ansong, J. K., Buijsman, M. C., Ciotti, R. B., Farrar, J., et al. (2018). A primer on global internal tide and internal gravity wave continuum modeling in HyCOM and MITgcm. In E. Chassignet, A. Pascual, J. Tintore, & J. Verron (Eds.), *New frontiers in operational oceanography* (pp. 307–391). Tallahassee, FL: GODAE OceanView. https://doi.org/10.17125/gov2018.ch13

Arbic, B. K., Richman, J. G., Timko, P. G., Metzger, E. J., & Wallcraft, A. J. (2012). Global modeling of internal tides within an eddying ocean general circulation model. *Oceanography*, *25*(2), 20–29. https://doi.org/10.5670/oceanog.2012.38

Arbic, B. K., Wallcraft, A. J., & Metzger, E. J. (2010). Concurrent simulation of the eddying general circulation and tides in a global ocean model. *Ocean Modelling*, *32*, 175–187. https://doi.org/10.1016/j.ocemod.2010.01.007

Benada, J. R. (1997). PO.DAAC Merged GDR (TOPEX/POSEIDON) Generation B User's Handbook. Retrieved from ftp://podaac.jpl.nasa.gov/allData/topex/L2/mgdrb/docs/uhmgdrb/html/usrtoc.htm

Buijsman, M. C., Arbic, B. K., Richman, J. G., Shriver, J. F., Wallcraft, A. J., & Zamudio, L. (2017). Semidiurnal internal tide incoherence in the Equatorial Pacific. *Journal of Geophysical Research: Oceans*, *122*, 5286–5305. https://doi.org/10.1002/2016JC012590

Colosi, J. A., & Munk, W. (2006). Tales of the venerable Honolulu tide gauge. *Journal of Physical Oceanography*, *36*(6), 967–996. https://doi.org/10.1175/JPO2876.1

Duda, T. F., Collis, J. M., Lin, Y.-T., Newhall, A. E., Lynch, J. F., & DeFerrari, H. A. (2012). Horizontal coherence of low-frequency fixed-path sound in a continental shelf region with internal-wave activity. *The Journal of the Acoustical Society of America*, *131*(2), 1782–1797. https://doi.org/10.1121/1.3666003

Dunphy, M., & Lamb, K. G. (2014). Focusing and vertical mode scattering of the first mode internal tide by mesoscale eddy interaction. *Journal of Geophysical Research: Oceans*, *119*, 523–536. https://doi.org/10.1002/2013JC009293

Dunphy, M., Ponte, A. L., Klein, P., & Le Gentil, S. (2017). Low-mode internal tide propagation in a turbulent eddy field. *Journal of Physical Oceanography*, *47*, 649–665. https://doi.org/10.1175/JPO-D-16-0099.1

Elipot, S., Lumpkin, R., Perez, R. C., Lilly, J. M., Early, J. J., & Sykulski, A. M. (2016). A global surface drifter data set at hourly resolution. *Journal of Geophysical Research: Oceans*, *65*, 29–50. https://doi.org/10.1002/2016JC011716

Fu, L.-L., Alsdorf, D., Morrow, R., Rodrigues, E., & Mognard, N. (2012). SWOT: The surface water and ocean topography mission—Wide-swath altimetric measurement of water elevation on Earth. *JPL Publication*, *12*(5), 228p. Retrieved from http://swot.jpl.nasa.gov/files/SWOT_MSD_final-3-26-12.pdf

Kelly, S. M., & Lermusiaux, P. F. J. (2016). Internal-tide interactions with the Gulf Stream and Middle Atlantic Bight shelfbreak front. *Journal of Geophysical Research: Oceans*, *121*, 6271–6294. https://doi.org/10.1002/2016JC011639

Kelly, S. M., Lermusiaux, P. F. J., Duda, T. F., & Haley, P. J. (2016). A coupled-mode shallow-water model for tidal analysis: Internal tide reflection and refraction by the Gulf Stream. *Journal of Physical Oceanography*, *46*, 3661–3679. https://doi.org/10.1175/JPO-D-16-0018.1

Kelly, S. M., Nash, J. D., & Kunze, E. (2010). Internal-tide energy over topography. *Journal of Geophysical Research*, *115*, C06014. https://doi.org/10.1029/2009JC005618

Klymak, J. M., Simmons, H. L., Braznikov, D., Kelly, S., MacKinnon, J. A., Alford, M. H., et al. (2016). Reflection of linear internal tides from realistic topography: The Tasman continental slope. *Journal of Physical Oceanography*, *46*, 3321–3337. https://doi.org/10.1175/JPO-D-16-0061.1

Luecke, C. A., Arbic, B. K., Bassette, S. L., Richman, J. G., Shriver, J. F., Alford, M. H., et al. (2017). The global mesoscale eddy available potential energy field in models and observations. *Journal of Geophysical Research: Oceans*, *122*, 9126–9143. https://doi.org/10.1002/2017JC013136

Madec, G. (2008). NEMO ocean engine. In *Note du Pôle de modélisation, Institut Pierre-Simon Laplace (IPSL)*, France. https://doi.org/10.5281/zenodo.3248739

Müller, M., Cherniawsky, J. Y., Foreman, M. G. G., & von Storch, J.-S. (2012). Global M_2 internal tide and its seasonal variability from high resolution ocean circulation and tide modeling. *Geophysical Research Letters*, *39*, L19607. https://doi.org/10.1029/2012GL053320

Ngodok, H. E., Souopgui, I., Wallcraft, A. J., Richman, J. G., & Shriver, J. F. (2016). On improving the accuracy of the M_2 barotropic tides embedded in a high-resolution global ocean circulation model. *Ocean Modelling*, *97*, 16–26. https://doi.org/10.1016/j.ocemod.2015.10.011

Pujol, M.-I., Faugère, Y., Taburet, G., Dupuy, S., Pelloquin, C., Ablain, M., & Picot, N. (2016). DUACS DT2014: The new multi-mission altimeter data set reprocessed over 20 years. *Ocean Science*, *12*(5), 1067–1090. https://doi.org/10.5194/os-12-1067-2016

Ray, R. D. (1998). Spectral analysis of highly aliased sea-level signals. *Journal of Geophysical Research*, *103*(C11), 24,991–25,003. https://doi.org/10.1029/98JC02545

Ray, R. D., & Mitchum, G. T. (1996). Surface manifestation of internal tides generated near Hawaii. *Geophysical Research Letters*, *23*(16), 2101–2104. https://doi.org/10.1029/96GL02050

Ray, R. D., & Mitchum, G. T. (1997). Surface manifestation of internal tides in the deep ocean: Observations from altimetry and tide gauges. *Progress in Oceanography*, *40*, 135–162. https://doi.org/10.1016/S0079-6611(97)00025-6

Ray, R. D., & Zaron, E. D. (2011). Non-stationary internal tides observed with satellite altimetry. *Geophysical Research Letters*, *38*, L17609. https://doi.org/10.1029/2011GL048617

Ray, R. D., & Zaron, E. D. (2016). M2 internal tides and their observed wavenumber spectra from satellite altimetry. *Journal of Physical Oceanography*, *46*, 3–22. https://doi.org/10.1175/JPO-D-15-0065.1

Richman, J. G., Arbic, B. K., Shriver, J. F., Metzger, E. J., & Wallcraft, A. J. (2012). Inferring dynamics from the wavenumber spectra of an eddying global ocean model with embedded tides. *Journal of Geophysical Research*, *117*, C12012. https://doi.org/10.1029/2012JC008364

Rocha, C. B., Chereskin, T. K., Gille, S. T., & Menemenlis, D. (2016). Mesoscale to submesoscale wavenumber spectra in Drake Passage. *Journal of Physical Oceanography*, *46*, 601–620. https://doi.org/10.1175/JPO-D-15-0087.1

Rocha, C. B., Gille, S. T., Chereskin, T. K., & Menemenlis, D. (2016). Seasonality of submesoscale dynamics in the Kuroshio Extension. *Geophysical Research Letters*, *43*, 304–311. https://doi.org/10.1002/2016GL071349

Savage, A. C., Arbic, B. K., Richman, J. G., Shriver, J. F., Alford, M. H., Buijsman, M. C., et al. (2017). Frequency content of sea surface height variability from internal gravity waves to mesoscale eddies. *Journal of Geophysical Research: Oceans*, *122*, 2519–2538. https://doi.org/10.1002/2016JC012331

Shriver, J. F., Arbic, B. K., Richman, J. G., Ray, R. D., Metzger, E. J., Wallcraft, A. J., & Timko, P. G. (2012). An evaluation of the barotropic and internal tides in a high-resolution global ocean circulation model. *Journal of Geophysical Research*, *117*, C10024. https://doi.org/10.1029/2012JC008170

Thoppil, P. G., Richman, J. G., & Hogan, P. J. (2011). Energetics of a global ocean circulation model compared to observations. *Geophysical Research Letters*, *38*, L15607. https://doi.org/10.1029/2011GL048347

Timko, P. G., Arbic, B. K., Richman, J. G., Scott, R. B., Metzger, E. J., & Wallcraft, A. J. (2012). Skill tests of three-dimensional tidal currents in a global ocean model: A look at the North Atlantic. *Journal of Geophysical Research*, *117*, C08014. https://doi.org/10.1029/2011JC007617

Timko, P. G., Arbic, B. K., Richman, J. G., Scott, R. B., Metzger, E. J., & Wallcraft, A. J. (2013). Skill testing a three-dimensional global tide model to historical current meter records. *Journal of Geophysical Research: Oceans*, *118*, 6914–6933. https://doi.org/10.1002/2013JC009071

Waterhouse, A. F., MacKinnon, J. A., Nash, J. D., Alford, M. H., Kunze, E., Simmons, H. L., et al. (2014). Global patterns of diapycnal mixing from measurements of the turbulent dissipation rate. *Journal of Physical Oceanography*, *44*(7), 1854–1872. https://doi.org/10.1175/JPO-D-13-0104.1

Zaron, E. D. (2015). Non-stationary internal tides inferred from dual-satellite altimetry. *Journal of Physical Oceanography*, *45*(9), 2239–2246. https://doi.org/10.1175/JPO-D-15-0020.1

Zaron, E. D. (2017). Mapping the nonstationary internal tide with satellite altimetry. *Journal of Geophysical Research: Oceans*, *122*, 539–554. https://doi.org/10.1002/2016JC012487

Zhao, Z., Alford, M. H., Girton, J. B., Rainville, L., & Simmons, H. L. (2016). Global observations of open-ocean mode-1 M_2 internal tides. *Journal of Physical Oceanography*, *46*, 1657–1684. https://doi.org/10.1029/2018JC014475

Zhou, X.-H., Wang, D.-P., & Chen, D. (2015). Validating satellite altimeter measurements of internal tides with long-term TAO/TRITON buoy observations at 2° S–156° E. *Geophysical Research Letters*, *42*, 4040–4046. https://doi.org/10.1002/2015GL063669

Erratum

In the originally published version of this paper, the captions for Figure 4 and Figure 5 were transposed as the result of a typesetting error. This error has been corrected, and this may be considered the official version of record.